

PAPER • OPEN ACCESS

## Combining active and passive acoustic methods to image hydraulic fracture growth in laboratory experiments

To cite this article: Seyyedmaalek Momeni *et al* 2021 *IOP Conf. Ser.: Earth Environ. Sci.* **833** 012088

View the [article online](#) for updates and enhancements.



### 240th ECS Meeting

Digital Meeting, Oct 10-14, 2021

**We are going fully digital!**

Attendees register for free!

**REGISTER NOW**



# Combining active and passive acoustic methods to image hydraulic fracture growth in laboratory experiments

Seyyedmaalek Momeni, Dong Liu, Brice Lecampion

Geo-Energy Lab - Gaznat chair on Geo-Energy, EPFL, Lausanne CH-1015

E-mail: brice.lecampion@epfl.ch

**Abstract.** We combine active and passive acoustic measurements to improve the spatio-temporal imaging of hydraulic fracture growth performed under true triaxial confinement in the laboratory. 64 active piezo-electric transducers (54 P waves, 10 S waves) work in source (32) - receivers (32) mode to perform an acoustic survey at repetitive intervals (every 10 seconds) during a hydraulic fracture growth experiment. The analysis of the evolution of the active acoustic monitoring changes allow to image the evolution of the fracture front (via an inversion of the active acoustic waves diffracted by the fracture front). An additional 16 piezoelectric transducers are pre-amplified and work in passive mode continuously recording at 10MHz. We present a nearly-automatic passive signal processing, acoustic emission detection, and location algorithm. This allows to record, detect and to locate acoustic emissions associated with fracture initiation and growth in between the active acoustic measurement sequences. Using a hydraulic fracturing test performed in gabbro, we discuss how active and passive acoustic monitoring complements one another and bring different type of information on hydraulic fracture growth.

## 1. Introduction

Hydraulic fractures are a class of tensile fractures that propagate in a material as a result of fluid pressurization. Investigation of the growth of such fluid-driven fractures under controlled conditions at the laboratory scale plays an important role in order to validate theoretical predictions. We combine active acoustic imaging and passive acoustic emission (AE) monitoring to capture the spatio-temporal evolution of hydraulic fracturing in rocks at the laboratory scale.

Active acoustic imaging is based on a 4D seismic survey at the laboratory scale in the ultrasonic range: an acoustic survey is repeated at regular intervals during the experiment. Earlier studies [1, 2, 3, 4, 5] have shown its capability to obtain quantitative information on fracture growth during laboratory hydraulic fracture experiments. The active wave-field can be diffracted by the fracture tip (as well as the fluid front if a lag is present near the fracture tip) and also reflected by and transmitted through the fluid-filled fracture. The time-evolution of the transmitted waves notably allows to identify a dry region near the fracture tip (fluid lag) [1, 2]. Records of the evolution of the arrival times of the active wave-fields diffracted by the fracture tip have enable to estimate the evolving fracture tip position under the hypothesis of a horizontal radial fracture centered on the injection point [5, 6]. The fluid layer thickness in the fracture (i.e. its opening) can also be estimated by matching the spectrum of the transmitted signals with the transmission coefficient of a three layers model, considering attenuation and delay of



transmitted waves [7]. The diffraction and transmission techniques have been shown to provide results in agreement with optical methods [8]. We have recently extended these active acoustic techniques increasing the number of sensors and improving the fracture front reconstruction algorithm [9].

In rocks, acoustic emission (AE) monitoring is widely used to track hydraulic fracture growth ([10, 11]). AE refers to the generation of transient elastic waves in a material caused by the sudden occurrence of fractures or frictional sliding along discontinuous surfaces ([12]). AE monitoring provides source locations of individual micro-ruptures occurring within an observable frequency bandwidth [13, 14, 15, 11, 16]. It is estimated that much of the fracture deformation and energy release throughout a hydraulic fracturing treatment is aseismic ([17, 18, 19]). Although AE observations do not provide the entire story behind a hydraulic fracturing treatment and are limited to energies released in a specified frequency range, they provide significant numbers of located events which help in imaging the fracture zone and understanding mechanisms of their source ruptures. They are also one of the most used markers to estimate the fracture initiation phase ([20, 21, 22]).

Some recent studies have partly combined active and passive monitoring techniques to obtain the spatio-temporal changes of elastic properties in porous rocks ([10, 23, 24]). However, the performance of the imaging system is intrinsically related to the design and number of sensors - especially to image macroscopic fracture. Here we show that combined active and passive acoustic monitoring with a dense active source/receiver pairs and passive AE monitoring network can yield a unique spatial and temporal imaging of hydraulic fracture growth in rocks.

## 2. Experimental methods

### 2.1. Poly-axial frame and injection system

Hydraulic fracture growth experiments are carried out in a 250 mm cubic rock sample under a true triaxial compressive state of stress as shown in Figures 1 and 2a. The confinement is applied by symmetric pairs of flat jacks in the three axis of a poly-axial reacting frame. Compressive stresses up to 20 MPa can be applied prior to injection. The fracturing fluid is injected in a central wellbore by a syringe pump (ISCO D160) at a constant flow rate (in the range 0.001 mL/min to 107 mL/min) with a maximum injection pressure of 51 MPa. An interface vessel in the injection line allows injecting a wide range of fluid types with viscosity ranging from 1 mPa.s to 1000 Pa.s. Due to the compliance of the injection system (associated with the volume of fluid in the injection line), upon fracture initiation, the flow rate entering the fracture does not equal the pump injection rate  $Q_o$  during a transient phase [25, 26]. A needle valve is thus placed in the injection line close to the well-head to control the release of fluid compressed during the pressurization phase. Using volume conservation within the injection system (pump to fracture inlet), the flow rate  $Q_{in}(t)$  entering the fracture can be estimated by taking the derivatives of the fluid pressure measurements [9].

### 2.2. Active acoustic measurement system

Active acoustic monitoring is integrated within the poly-axial cell. 64 piezoelectric transducers are included in the loading platens: 32 transducers act as sources and 32 as receivers. This array of transducers consists of 10 shear-wave transducers and 54 longitudinal-wave ones. We use a source function generator connected to a high-power amplifier to send a Ricker excitation signal with a given central frequency that can be set between 300 and 750 kHz depending on the material type. The source signal is routed to one of the 32 source transducers via a multiplexer. The 32 receiver transducers are connected to a high-speed acquisition board in order to record the signal simultaneously on all receivers with a sampling frequency of 50 MHz. As the switch between sources is limited by the multiplexer, the excitation of a given source is repeated 50 times, and the data stacked to improve the signal to noise. Spanning of the 32 sources defines

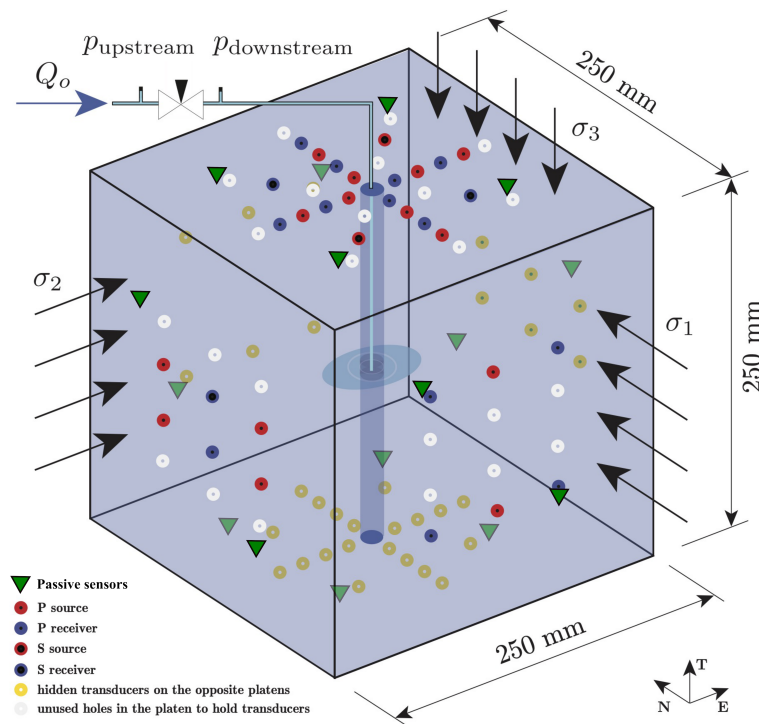


**Figure 1.** Schematic illustration of the rock sample showing the active and passive transducers disposition for the GABB-006 experiment (Adapted from [9]). Additional holes are available in the platens allowing the use of various transducer dispositions. Two facing platens share the same transducers disposition and source-receiver transducers are alternately located on opposite platens for robustness.

an acquisition sequence and takes about 2.9 seconds in total. For all source-receiver pairs, the recorded signal at given time during the experiment is subtracted from the one of an initial survey recorded at the beginning of the experiment prior to fracture initiation. The evolution of these active acoustic changes for each source-receiver pair are sorted with respect to their acquisition times, and the evolution of the arrival time of the diffracted wave by the fracture are manually picked (see Figure 2b). The knowledge of the arrival time of the diffracted wave for a number of different source-receiver pairs allow to reconstruct the fracture front. We refer to [9] for the details of the solution of this inverse problem which is performed independently for every active survey performed during the experiment.

In addition to acoustic data, we record fluid injection pressure (upstream and downstream the needle valve), volume and pressure of each flat-jack pairs at 1 Hz. All the measurements are synchronized via a dedicated LabView application [9].

### 2.3. Passive acoustic measurement system

Our passive AE monitoring network consists of 16 Vallen VS150-M resonant piezoelectric sensors that record AEs in a continuous mode with a sampling rate of 10 MHz (Fig. 1). They record AEs in the frequency range 100 KHz to 400 KHz with a peak of resonance at 150 KHz. Each passive sensor is connected to a pre-amplifier to increase the signal to noise ratio. The signals are then recorded after digitalization using a Labview application. Four passive sensors are set on each of the top and bottom platens while each vertical platen contains two sensors. Similarly than for the active sensors, each passive sensor is pushed to the specimen by a spring set behind



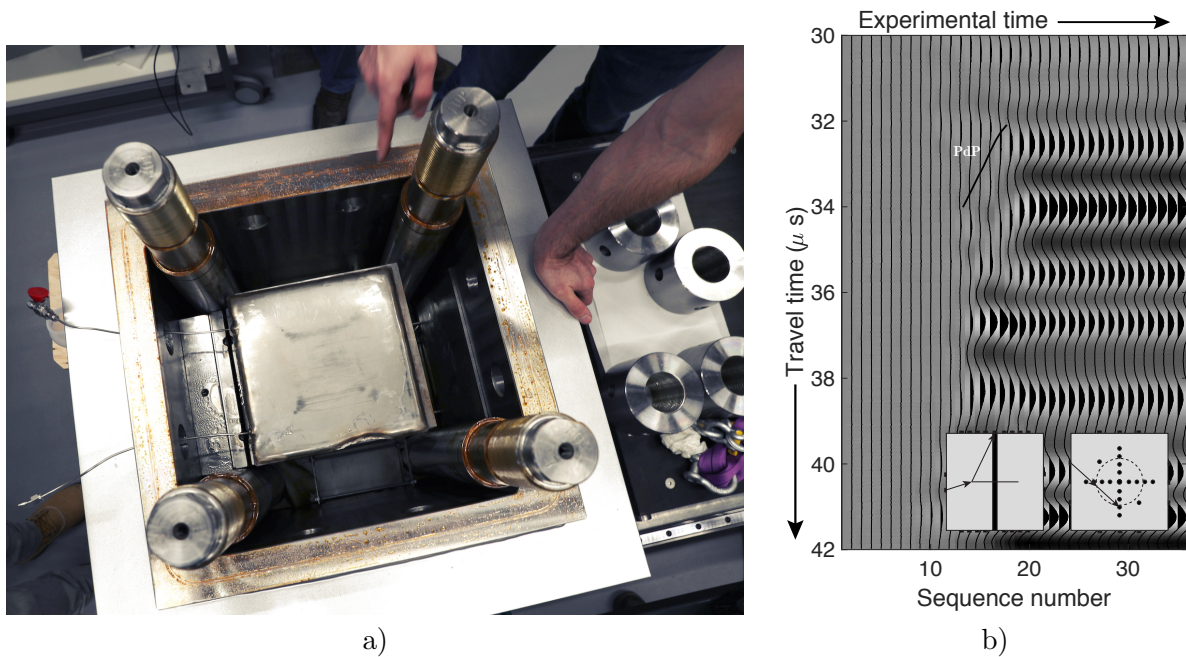


**Figure 2.** a) Top view of the poly-axial frame, b) illustration for a given source-receiver pair of the evolution of the diffracted wave pattern recorded during the GABB-006 experiment with the active acoustic system (the black line marked PdP shows the manually picked arrival times).

**Table 2.** Sample dimensions and wave velocities for the GABB-006 experiment.  $V_p$  and  $V_s$  are measured directly with the cubic rock sample during the pressurization stage prior to fracture initiation. The fracture initiates 9.5 mm below the notch position.

| $V_p$ (m/s)        | $V_s$ (m/s)        | Block size (mm)             | Notch position (mm) |
|--------------------|--------------------|-----------------------------|---------------------|
| $6734.5 \pm 168.4$ | $3668.9 \pm 196.5$ | $250 \times 250 \times 249$ | 124                 |

them inside the loading platens. The coupling between sensors and specimen is provided using a coupling contact gel.

### 3. A hydraulic fracture experiment in Gabbro

We report here the results of a hydraulic fracturing test performed in gabbro where glycerol was injected at a rate of 0.05mL per minute. The material properties and acoustic waves velocities of this gabbro are reported in Tables 1 and 2, while the details of the configuration of the experiment are listed in Table 3. The propagation duration as well as the estimated time-scales respectively for the transition from the viscosity to the toughness dominated regime ( $t_{mk}$ ) and the disappearance of the fluid lag ( $t_{om}$ ) are listed in Table. 4. The propagation time is much larger than the viscosity to toughness transition time-scale  $t_{mk}$  which ensures that this experiment lies in the so-called toughness dominated regime of growth (see [26] for details).

**Table 1.** Rock properties. Porosity represents the connected volume porosity measured using a gas pycnometer. Elastic properties have been measured on tri-axial tests under quasi-static loading.

| Rock            | $E$ (GPa) | $\nu$ | $\rho$ ( $\times 10^3 \text{kg/m}^3$ ) | Grain size (mm) | Porosity (%) |
|-----------------|-----------|-------|--|-----------------|--------------|
| Zimbabwe gabbro | 99.7      | 0.29  | 3.00                                   | 1-3             | 0.32         |

**Table 3.** Sample configuration and experimental parameters for HF injection in GABB-006. The system compliance  $U$  is calculated from the initial linear pressurization phase (prior to fracture initiation) knowing the injection rate  $Q_o$ .

| Fracturing fluid | $\sigma_3$ (MPa) | $\sigma_1 = \sigma_2$ (MPa) | Injection rate $Q_o$ (mL/min) | System compliance $U$ (mL/GPa) |
|------------------|------------------|-----------------------------|-------------------------------|--------------------------------|
| Glycerol         | 10               | 20                          | 0.04                          | 225.9                          |

**Table 4.** Characteristic timescales for the GABB-006 experiment: viscosity–toughness transition  $t_{mk}$ , and fluid lag disappearance timescale  $t_{om}$ . We estimate these timescales using the averaged entering flow rate into the fracture  $\langle Q_o \rangle$  estimated during the fracture duration  $t_{prop}$  and  $K_{Ic} = 3.03 \text{ MPa.m}^{1/2}$  [27].

| $\langle Q_o \rangle$ (mL/min) | Propagation duration $t_{prop}$ (s) | $t_{mk}$ (s)         | $t_{om}$ (s) | Propagation regime  |
|--------------------------------|-------------------------------------|----------------------|--------------|---------------------|
| 0.2769                         | $\approx 183$                       | $3.2 \times 10^{-2}$ | 85.3         | toughness dominated |

### 3.1. Low frequency measurements

The time evolution of the fluid pressure upstream and downstream the valve, that of the inlet flux, fracture front extent (reconstructed from the diffracted waves) are displayed in Fig. 4. The fracture front reconstructed from the diffracted waves via an elliptical and a circular model are displayed in Fig. 3a for the different active acoustic surveys performed during the experiment. The created fracture is clearly visible on the photo of the block cut after the test (see Fig. 3b).

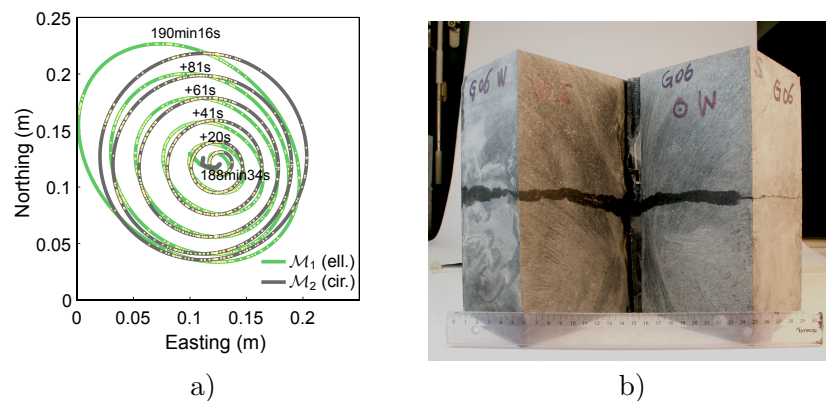


**Figure 3.** GABB-006: a) Top-view of the fracture footprint estimated from diffracted waves from a and b) picture of the block cut after the test with a visible hydraulic fracture. The yellow dots in figure a) indicate the diffractors at the fracture front for the different source–receiver pairs picked. M1 and M2 are the estimated fracture front geometries using an elliptical and a circular geometry respectively (see [9] for details on the inverse problem methodology).

### 3.2. Passive acoustic monitoring

Continuous acoustic signals that were recorded with 16 piezoelectric sensors are first processed as follow: removing mean and trend, filtering, wavelet denoising). The AEs P-wave arrival phases are then detected using STA/LTA algorithm ([28]). The detected phases are associated to create potential AEs, knowing the maximum distance between AE source and receivers in the specimen and the P-wave velocity that measured from active measurements. We categorize the phases that have arrival time differences in this range as potential events.

The probable arrival times of all potential event phases are read using our defined algorithm. This algorithm adopts STA/LTA and Aikake Information Criteria (AIC) [29] algorithms on a

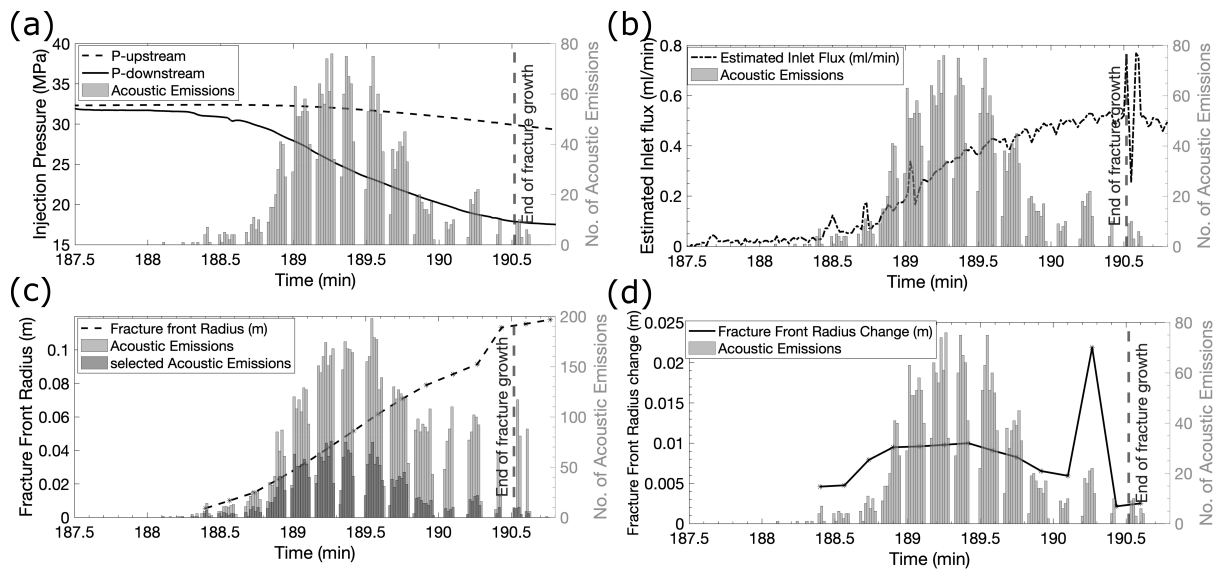


**Figure 4.** Time distribution of AEs versus upstream and downstream pressure (a), inlet flux (b), fracture front radius (c), and fracture front radius change (d) estimated by the active acoustic measurements. The systematic gaps in the reported number of AEs are due to the active shots that saturate the passive AE signals.

short time window of the P-wave phase arrival to detect the probable arrival times. The sum of absolute amplitudes of each signal before and after each potential arrival time is then compared. The one with the maximum change is selected as the preferred arrival time. A smoothed envelope is created for each signal in order to help narrowing the arrival time search window and speed up the phase picking algorithm. We define weights for the accuracy of each P-wave arrival-time reading based on their changes in amplitudes before and after each arrival time. This means that weaker signals on some sensors will have smaller contribution in the localization of that event.

A two-steps 3D grid search localization algorithm is adopted for event localization. First, a coarse grid is defined inside the specimen with a spatial resolution of one centimeter. The travel time differences for each defined trial source and related receiver pairs are first computed off-line. They are then compared to the actual travel time differences of each potential AE. The location having the smallest RMS for the travel time differences is chosen as the preferred one. After finding the AE location with a resolution of one centimeter, the algorithm is repeated on a finer grid with one millimeter resolution in a two centimeters radius region from the previously obtained location.

Applying this method on the 3 minutes of continuous data recognized as the fracture propagation period by the active method, we locate > 8800 AEs. Among them, to have reliable locations, we select AEs that are recorded in at least eight sensors, have azimuthal gap of less than 180° and a RMS less than 3 microseconds. The new set contains 2500 AEs. Their distribution in time together with the upstream and downstream pressures, estimated inlet flux, fracture front radius, and fracture front radius change are shown in Figure 4 and their evolution with fracture front steps obtained from active acoustic measurements is presented in Figure 5.

We observe that the number of AEs has increased before the strong drop observed in the downstream pressure and continued until the fracture front reach the end of the specimen. The observed peak in AE distribution at the end of the fracture completion is interpreted as the breakage of a bridge situated on the fracture plane.

The snapshots in Figure 5 show that the fracture has initiated slightly below the notch, which

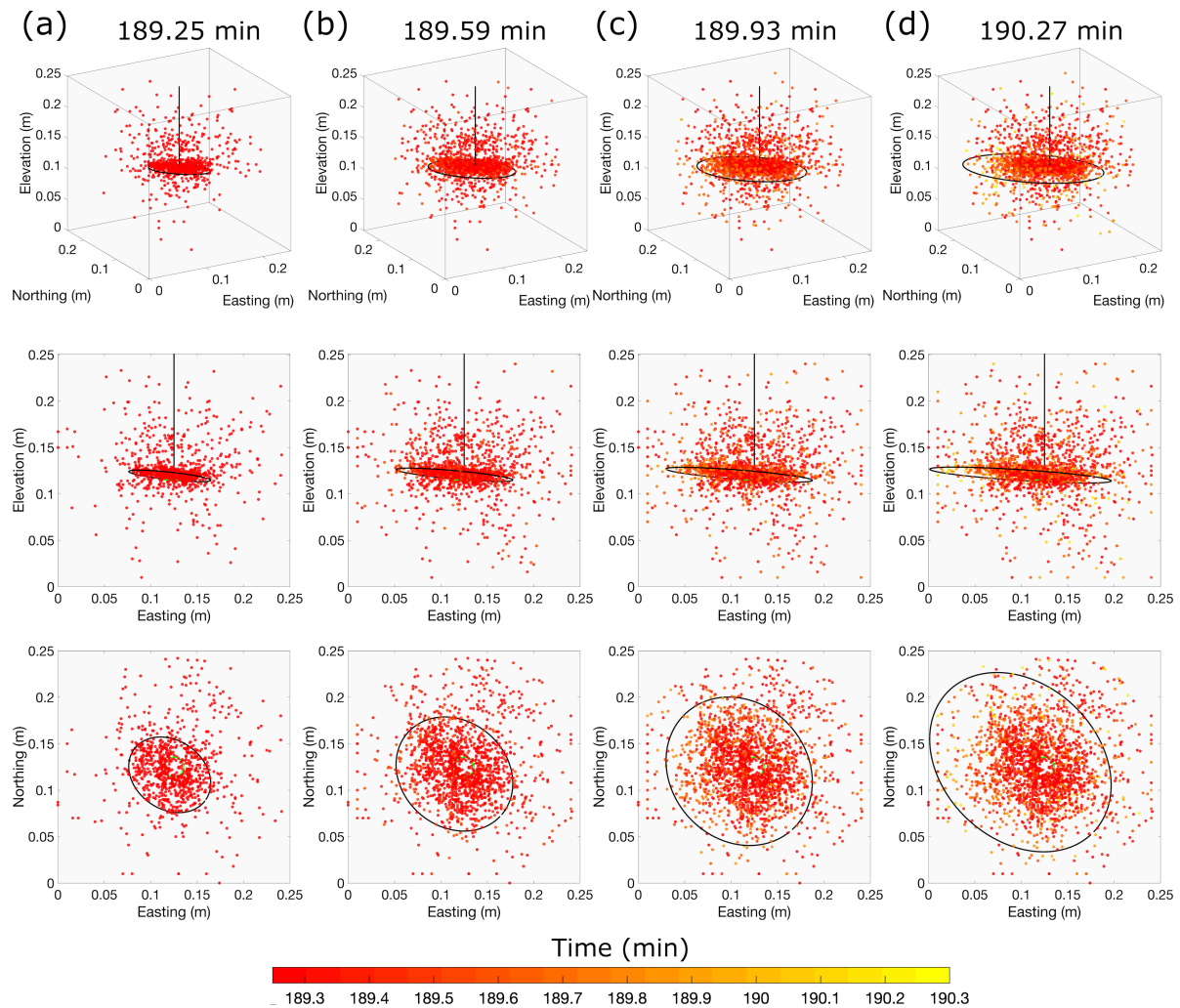


**Figure 5.** Snapshots of the spatio-temporal distribution of hydraulic fracture growth and occurred AEs during the GABB-006 experiment at four distinct times. Black lines show the injection line. Black ellipses represent the fracture fronts estimated from the active acoustic measurement at the specific time, while colored circles are the AEs occurred up to that time. The three rows show different views from angle, east, and top, respectively.

is consistent with the fracture front reconstructed from the active imaging method and the direct post-test visual inspection (Fig. 3b).

#### 4. Conclusions

Combining active and passive acoustic monitoring techniques during hydraulic fracturing experiments has allowed us to capture the spatial and temporal evolution of the fracture growth at millimeter resolution. These data are extremely valuable in order to understand the main parameters controlling hydraulic fracturing (various confining stress, injection rate) and in rocks. The Gabbro experiment presented here exhibits a toughness dominated propagation where most of the energy is spent in the creation of new fracture surfaces [30]. The fracture initiation is detected by a clear drop in the downstream fluid pressure, fluctuation in the estimated inlet flux, as well as the rise of the number of AEs localized near the injection point. The fracture front is reconstructed using an elliptical geometrical model from the arrival of the diffracted active P waves recorded during each active survey performed every 10 seconds during the test. We

note that in this measurement system, the active data for one acquisition sequence are acquired in about 2.9 seconds such that this imaging technique is appropriate for fractures propagating at mm/sec velocities. The average fracture growth velocity for the reported gabbro test is of 0.69 mm/sec. The intrinsic spatial resolution of the active acoustic reconstruction of the fracture front is thus of about 2mm. The results shows a growth of the fracture toward the Northwest (Figure 5). The estimated fracture plane has a dip of 13° toward the Southeast. The reconstructed fracture front evolution from the active acoustics surveys and the concentration of localized passive AEs are in good agreement.

We observe a direct relationship between the fracture front acceleration and the number of AEs (Figure 4 d). A reduction in the velocity of the fracture front radius at about 189.4 minutes followed by a decrease in the number of AEs. The fracture front reaches the western end of specimen at about 190.25 minutes and that is observable from the large fluctuation in the estimated inlet flux as well as a sudden increase in the reconstructed fracture radius front.

A number of AEs are detected prior to the first fracture front reconstructed from the active acoustic measurement (Figure 4c). The Gaussian distribution of AEs is obvious in Figure 4. Gaps in the number of localized AEs can be observed when an active measurement sequence is performed as the signal saturates on the passive sensors (Figure 4c & d). A few AEs happened after the fracture front reaching the edge of the block at 190.3 minutes, probably related to the closing of the fracture. The number of AEs decay in parallel with the pressure decay and with the drop of the fracture front velocity (estimated from the active measurements), in line with the propagation of the radial fracture (Figures 4 and 5).

## References

- [1] Medlin W and Masse L 1984 *SPE Journal* **24** 256–268
- [2] De Pater C, Desroches J, Groenenboom J and Weijers L 1996 *SPE Production & Facilities* **11** 122–128
- [3] Glaser S D and Hand M K 1998 *Geotechnical Testing Journal* **21** 317–327
- [4] van Dam D B 1999 *The influence of inelastic rock behaviour on hydraulic fracture geometry* Ph.D. thesis TU Delft, Delft University of Technology
- [5] Groenenboom J and van Dam D B 2000 *Geophysics* **65** 603–611
- [6] Groenenboom J and Falk J 2000 *Geophysics* **65** 612–622
- [7] Groenenboom J and Fokkema J T 1998 *Geophysics* **63** 139–148
- [8] Kovalyshen Y, Bungler A P, Kear J and Kasperczyk D 2014 *International journal of rock mechanics and mining sciences* **70** 368–374
- [9] Liu D, Lecampion B and Blum T 2020 *Geophys. J. Int.* **223** 180–196
- [10] Stanchits S, Burghardt J and Surdi A 2015 *Rock Mechanics and Rock Engineering* **48** 2513–2527 ISSN 1434-453X
- [11] Hampton J, Gutierrez M, Matzar L, Hu D and Frash L 2018 *Journal of Rock Mechanics and Geotechnical Engineering* **10** 805–817 ISSN 1674-7755
- [12] Moore J R and Glaser S D 2007 *Journal of Geophysical Research: Solid Earth* **112**
- [13] Shapiro S A, Dinske C and Rothert E 2006 *Geophysical Research Letters* **33**
- [14] Eisner L, Gei D, Hallo M, Opršal I and Ali M Y 2013 *Geophysics* **78** A45–A49
- [15] Warpinski N 2009 *Journal of Petroleum Technology* **61** 80–85 ISSN 0149-2136
- [16] Ma X, Li N, Yin C, Li Y, Zou Y, Wu S, He F, Wang X and Zhou T 2017 *Petroleum Exploration and Development* **44** 1030–1037 ISSN 1876-3804
- [17] Maxwell S C, Waltman C, Warpinski N R, Mayerhofer M J and Boroumand N 2009 *SPE Reservoir Evaluation & Engineering* **12** 48–52 ISSN 1094-6470
- [18] Warpinski N R, Du J and Zimmer U 2012 Measurements of hydraulic-fracture-induced seismicity in gas shales sPE-151597-MS
- [19] Zhang Z, Rector J W and Nava M J 2018 *Geophysics* **83** KS1–KS10
- [20] Mazal P, Vlasic F and Koula V 2015 *Procedia Engineering* **133** 379–388 ISSN 1877-7058 fatigue Design 2015, International Conference Proceedings, 6th Edition
- [21] Stanchits S, Surdi A, Gathogo P, Edelman E and Suarez-Rivera R 2014 *Rock Mechanics and Rock Engineering* **47** 1521–1532 ISSN 1434-453X
- [22] Tan J, Xie J, Li L, Lyu Q, Han J and Zhao Z 2020 *Geofluids* **2020** 8845292 ISSN 1468-8115
- [23] Brantut N 2018 *Geophysical Journal International* **213** 2177–2192 ISSN 0956-540X

- [24] Aben F M, Brantut N, Mitchell T M and David E C 2019 *Geophysical Research Letters* **46** 7337–7344
- [25] Lhomme T, Detournay E and Jeffrey R G 2005 *Strength, fracture and complexity* **3** 149–162
- [26] Lecampion B, Desroches J, Jeffrey R G and Bungler A P 2017 *Journal of Geophysical Research: Solid Earth* **122** ISSN 2169-9356
- [27] Meredith P and Atkinson B 1985 *Physics of the Earth and Planetary Interiors* **39** 33–51
- [28] Withers M, Aster R, Young C, Beiriger J, Harris M, Moore S and Trujillo J 1998 *Bulletin of the Seismological Society of America* **88** 95–106 ISSN 0037-1106
- [29] Akaike H 1974 *Annals of the Institute of Statistical Mathematics* **26** 363–387 ISSN 1572-9052 URL <https://doi.org/10.1007/BF02479833>
- [30] Detournay E 2016 *Annual Review of Fluid Mechanics* **48** 311–339